# Using optical fiber sensors for health monitoring of rotational systems

Hasib Alian[1], Shlomi Konforty[2], Uri Ben-Simon[3], Renata Klein[4], Moshe Tur[5] and Jacob Bortman[2]

[1]IAF – Israel Air Force
hasibalian@gmail.com

[2] PHM Lab, Department of Mechanical Engineering, Ben-Gurion University of the Negev, P.O. Box 653, Beer Sheva 84105, Israel
shlomiko@post.bgu.ac.il
jacbort@bgu.ac.il

[3] Israel Aerospace Industries, Israel
ubensimon@iai.co.il

[4] R.K. Diagnostics, Gilon, P.O.B. 101, D.N. Misgav 20103, Israel
renata.klein@rkdiagnostics.co.il

[5] School of Electrical Engineering, Tel Aviv University, Ramat Aviv 69978, Israel
tur@post.tau.ac.il

## Abstract

Health monitoring of rotating systems are based on the analysis of vibration signals. This research investigates the potential of using an optical fiber sensor of the Fiber Bragg Grating (FBG) type for the purpose of bearing prognostics, using strain measurements. Due to its small dimensions, FBG sensor can be embedded close to, or even inside the bearing. Moreover, it provides adjustable sensitivity, adjustable bandwidth, and immunity to electromagnetic interference. By placing miniature sensors in the immediate proximity of the bearing, the signal-to-noise ratio of the bearing strain signals is considerably enhanced and the transmission path effects are reduced.

The capabilities of FBG sensors for diagnostic of ball bearings were demonstrated by seeded tests. This demonstration was extended to monitor bearings during fatigue endurance tests. Sensitivity to FBG sensor location was studied and it was found that at all housing measuring points, the sensitivity was acceptable. The best sensitivity was found to be at the closest location to the fault.

The optical sensor was found to enable diagnostics of spall-like faults in the outer race with a very good discrimination power. In some cases estimation of the fault size was possible with a very high accuracy.

## 1 Introduction

Condition monitoring is the process of tracking and assessing the health of critical machines, based on the detection, diagnostics and prognostics of a failure. Bearings are critical elements of rotating machinery. They are used to support moving parts and decrease the friction between rotating components. While in wide use, bearings are prone to unexpected failures that can result in irreversible damage.

Detection, diagnostics and prognostics of damage in bearings have attracted considerable attention in the last decades; two examples are the early work of Sawalhi & Randall [3] and Heng, Zhang, Tan and Mathew [2]. Based on the characteristics of the impulse, Kogan, Bortman and Klein [4] suggested a vibration signal

processing algorithm for fault width estimation based on the dynamic behavior of a general bearing model. Their results were validated in seeded tests for faults wider than 1.1 mm, the algorithm shows satisfactory results, with errors below 15%.

The difficulty in bearing monitoring is caused by the presence of high vibrations excited by other parts in the machine, while the vibrations originating from the faulty bearing are much weaker. Moreover, the vibration sensors are often installed on the case, far from the fault in the bearing. This may affect the capability to detect vibrations from incipient bearing faults. The stronger and cleaner the signals, the more reliable are the estimated severity and location of the damage. Therefore, in vibrations, complex algorithms of signal processing are required for separation of sources of excitation.

Previous work by M Khmelnitsky, J Bortman, et al. [5] demonstrated that the closer the location of the sensor to the bearing defect the easier is the detection. Ref. [5] also shows the promising potential of using sensors made of optical fibers. Specifically, silica-based Fiber Bragg Grating (FBG) sensors (to be described below and see Kersey, Davis, et al. [6]) were used, having the following advantages over electrical-based sensors: (*i*) they are very thin (<200 microns) and can be placed very close to the sensed bearing; (*ii*) Silica is dielectric and immune to electromagnetic interference nor does it disturb other electrical-based sensors in its vicinity; (*iii*) FBG allows the sensing of both strain and temperature and there methods to differentiate between these two measurands; (iv) FBGs are accurate and reliable [10]; (*v*) Optical fibers are easily attached to or embedded in the bearing case; and finally (vi) FBGs can be multiplexed so a few tens of them can be placed on the same strand of optical fiber, allowing multiple sensing point with a single remotely interrogated fiber. Therefore, recently fiber-based sensing can be found in an increasing number of applications in structural health monitoring, replacing or augmenting other strain, temperature and vibration sensors.

In view of their many advantages and their ability to provide a signal whose contents is mostly determined by the bearing vibrations, rather than being influenced by remote irrelevant and disturbing sources of mechanical noise, it is our goal to clearly demonstrate the capabilities of FBG sensors to clearly monitoring bearing defects, including the determination of their sizes.

This paper is organized as follows: In section 2, a brief description of the FBG sensor is provided. Section 3 includes description of the experiments, test setup, position of the fibers and the defect locations. Section 4 presents the test results including a comparison between healthy and faulty bearing results and the techniques for detection of spalls. Section 5 suggests a method to measure the spall width using the FBG signals. In addition the effect of the load to these signals is presented. Finally the summary and conclusions are presented in section 6.

# 2 FBG sensor background

A FBG sensor comprises a short (a few millimeters) periodic perturbation of the refractive index along the core of a single mode optical fiber. This periodic corrugation with a period of $\Lambda$ and refractive index $\bar{n}$, Figure 1, selectively reflects light in a narrow band of wavelengths around the Bragg wavelength of peak reflection, $\lambda_0$, which is given by [6,7,8]:

$$\lambda_B = 2\bar{n}\Lambda_{FBG} \tag{1}$$

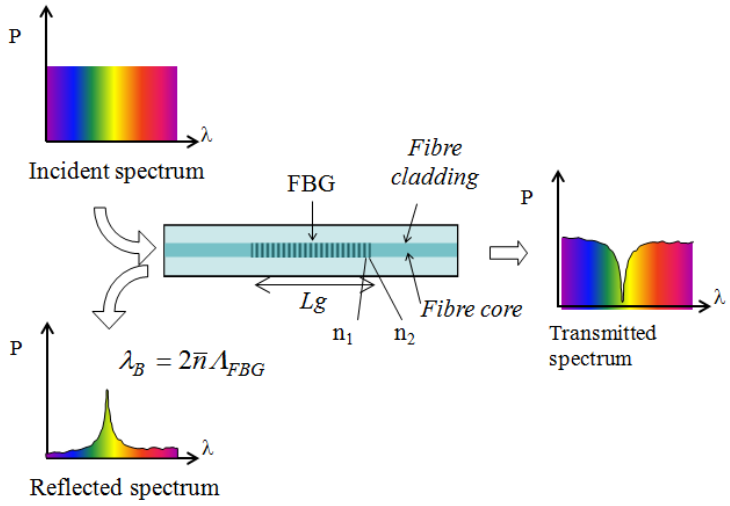


Figure 1: A FBG structure, with spectral response [8]

Since the strain and/or temperature affect both Λ and $\bar{n}$, these two measures shift the wavelength of the peak reflection from an appropriately chosen reference value, $\lambda_0$ according to:

$$\frac{\Delta\lambda}{\lambda_o} = C_\varepsilon \varepsilon + C_T \Delta T \qquad (2)$$

where $\varepsilon$ is the strain, $\Delta\lambda = \lambda_i - \lambda_0$, $\lambda_i$ is the shifted wavelength, $C_\varepsilon$ and $C_T$ are material constants, and $\Delta T$ is the temperature change. For germane-silicate single-mode fibers, working around 1550 nm, $C_\varepsilon = 0.788$ and $C_T = 8 \cdot 10^{-3} [/\,°C]$ ($C_T$ depends on the fiber coating).

As mentioned above, FBG sensors are easily multiplexed on the same strand of fiber. Using UV exposure and phase masks (or other techniques) tens of FBGs, each written with a different Λ, are generated, producing multiple and different reflection peaks { $\lambda_0$ }.

# 3 Experiments

The main goal of this work is to demonstrate the FBG sensor capability to monitor a bearing defect. Around 100 experiments in different conditions have been performed to investigate the efficiency of FBG sensors to diagnose spall-like faults on the bearing outer race.

## 3.1 Test set-up

The experimental system includes two subsystems; a generic test-rig (Figure 2) and a measurement unit.

The generic test-rig (Figure 2), includes an AC motor mounted by a standard coupling and connected to a shaft with two flywheels. The flywheels were used to create static loads on the bearings. Two identical bearings were mounted in bearing houses as shown in Figure 2. The monitored bearing was placed in the right bearing house.

The measurement unit includes a magnetic tachometer and optic fibers installed on the bearing housing. A commercial FBG interrogator was used and means were provided to synchronize the signals from the tachometer with those from the FBGs. Data were acquired at a rate of 10 Ksample/sec

The FBG interrogator used in the experiments uses a tunable laser, capable of scanning some tens of nanometers around the wavelength of 1550nm. By monitoring the power of the reflected light it finds and reports the locations of the peaks of the different FBGs along the fiber. Proper design of those reference wavelengths, taking into account the expected spectral shifts (fairly small in these experiments), ensures valid results. By comparing the measured peaks under strain with their initial values, one can calculate the

induced spectral shifts. Using equation (2) the strain can be determined. Indeed, there is a need to monitor the temperature when it changes throughout the experiment. In short measurements, it is the strain and not the temperature that mostly affects the spectral shifts.

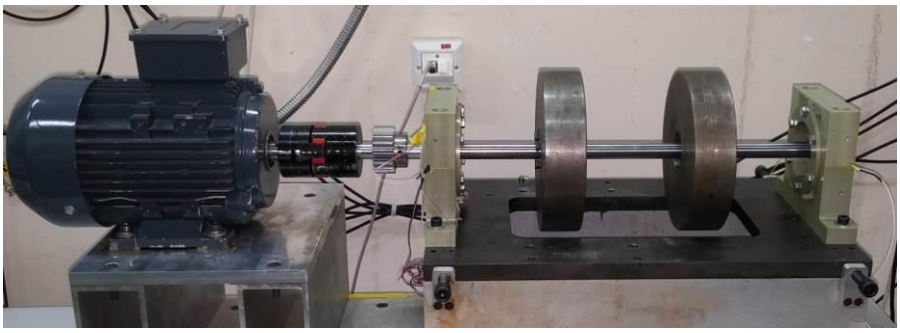

Figure 2: Test rig. The monitored bearing on the right side far from the motor

## 3.2 Fiber sensors positions

Two methods to install the fiber sensors were tested. The first, M1, aiming at minimizing the effects of the transfer path between the outer race and the sensors, was based on implanting one fiber with five sensors into the bearing house. This method requires machining around the bore diameter of the bearing house and implanting the fiber. The second method, M2, aiming at examining the possibility to install the fibers without the need to change the bearing house, was based on installing two fibers with three sensors each on top of the bearing house.

Figure 3 and Table 1 shows the sensors codes and locations. The sensor code consists of the letter S and an index (1 to 11), and also the installation method marked as M1 or M2 respectivly.

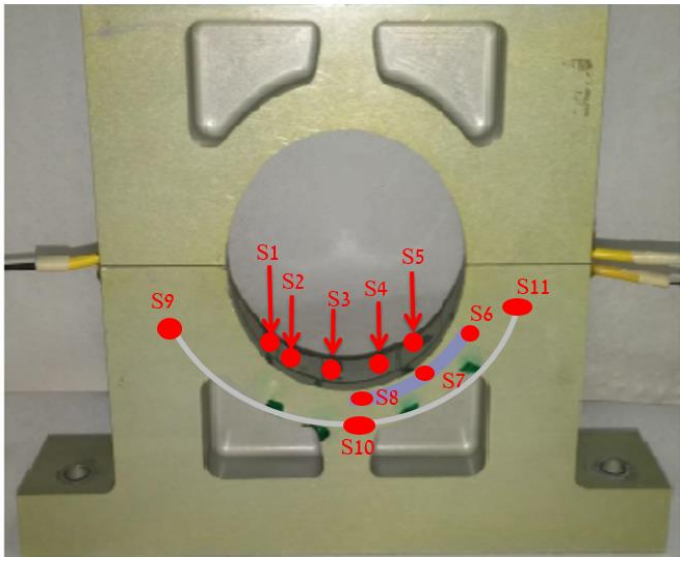


Figure 3: Sensors locations on the bearing house

| Sensor index | Installation method | Distance from the outer race[mm] |
|---|---|---|
| S01 | M 1 - implanting the fiber into the bearing house | 0 |
| S02 | M 1 - implanting the fiber into the bearing house | 0 |
| S03 | M 1 - implanting the fiber into the bearing house | 0 |
| S04 | M 1 - implanting the fiber into the bearing house | 0 |
| S05 | M 1 - implanting the fiber into the bearing house | 0 |
| S06 | M 2- installing fibers on the bearing house | 0.4 |
| S07 | M 2- installing fibers on the bearing house | 0.4 |
| S08 | M 2- installing fibers on the bearing house | 0.4 |
| S09 | M 2- installing fibers on the bearing house | 1.5 |
| S10 | M 2- installing fibers on the bearing house | 1.5 |
| S11 | M 2- installing fibers on the bearing house | 1.5 |

Table 1: List of the sensors

## 3.3 Bearings

Rolling element bearings are critical for proper function of rotating machines. They are used to support moving parts and decrease the friction between rotating components. The rolling element bearing consists of two ball races separated by balls, the inner race supports the shaft, while the outer race is typically press-fit into a bore. The balls are held in a cage.

Spalls on the races are one of the typical faults in bearings. A local fault on the outer race will generate an impulse every time the rolling element is in contact with the fault. The rate of impulses when the fault is on the outer race is defined by the BPFO (Ball Pass Frequency of the Outer race):

$$BPFO = \frac{n \cdot (f_i - f_0)}{2}\left(1 - \frac{d}{D}\cos(\alpha)\right) \qquad (3)$$

where: $n$ is the number of rolling elements, $f$ is the rotation frequency of the rings, $\alpha$ is the contact angle and $i, o$ indices represent inner and outer rings.

A set of six bearings SKF 6208 ETN9 (BPFO = 3.6) were monitored; a healthy bearing and five bearings with seeded faults of different widths on the outer ring; 0.39mm, 0.61mm, 1.12mm, 1.64mm and 2.64mm. The faults were produced by using EDM (Electrical Discharge Machining). Figure 4 shows one of the seeded faults.

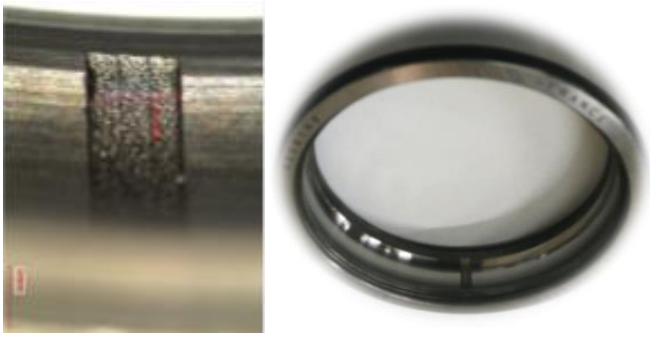

Figure 4: Outer ring with sedded defect

### 3.4 Defect location

The bearings have been installed with different fault locations. Three different locations have been considered as shown in Figure 5 (fault at 6, 4 and 8 o'clock).

Position 6 o'clock is in the center of the bearing loading zone. Positions 4 and 8 o'clock are considered out of the loading zone.

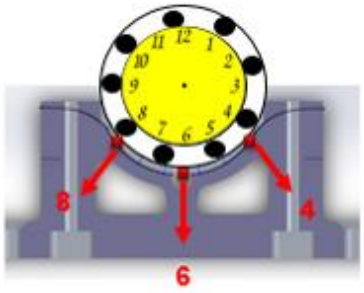


Figure 5: Defect location

### 3.5 Runs description

Around 100 runs were carried out at three different rotating speeds (20rps, 40rps and 60rps) with bearings in various conditions including healthy and faulty bearings in three different positions. Each condition was measured for at least 3 times. The runs are listed in the Table 2:

| Defect size [mm] | Defect location [-] | Rotating speed [Rps] | Sampling rate [Ksample/sec] | Fiber installation method |
|---|---|---|---|---|
| healthy | - | 20,40,60 | 10 | M1, M2 |
| 0.39mm | 4,6,8 | 20,40,60 | 10 | M1 |
| 0.61mm | 4,6,8 | 20,40,60 | 10 | M1 |
| 1.12mm | 4,6,8 | 20,40,60 | 10 | M1, M2 |
| 1.64mm | 4,6,8 | 20,40,60 | 10 | M1, M2 |
| 2.64mm | 4,6,8 | 20,40,60 | 10 | M1, M2 |
| 1.12mm | 6 | 20,40,60 | 20 | M2 |

Table 2: The runs data

## 4 Test results

The main goal of this work is to demonstrate the ability to diagnose faults in radial bearings using FBG sensors. The experiments had two goals: comparison between the methods of sensors installation, and evaluation of diagnostic capabilities based on strain measurements from optical fibers.

### 4.1 Rolling element and spall interaction

For better understanding of the rolling element behavior during the interaction with the spall, a rigid body dynamic bearing model suggested by G. Kogan, et al. [11] was used. The model produces a complete numerical simulation of the outer ring acceleration signal as a function of the shaft angle.

Figure 6 shows a typical acceleration signal during a non-continuous rolling element-spall interaction. The simulation assumes a small spall that does not allow contact between the rolling element and the spall floor. The interaction begins with the rolling element approaching the leading edge, the entrance zone represented in the model by $\Delta_{Dis}$. Following this, the rolling element disconnects from the leading edge and

performs a free flight represented by $\Delta_{imp}$, the free flight ends when the rolling element collides with the trailing edge. After the first collision, the rolling element rattles between the raceways several times. This rattling continues until the rolling element is locked between the raceways and exits the spall. The rattling zone is represented by $\Delta_{TE}$. Each rattle generates an impulse of high frequency.

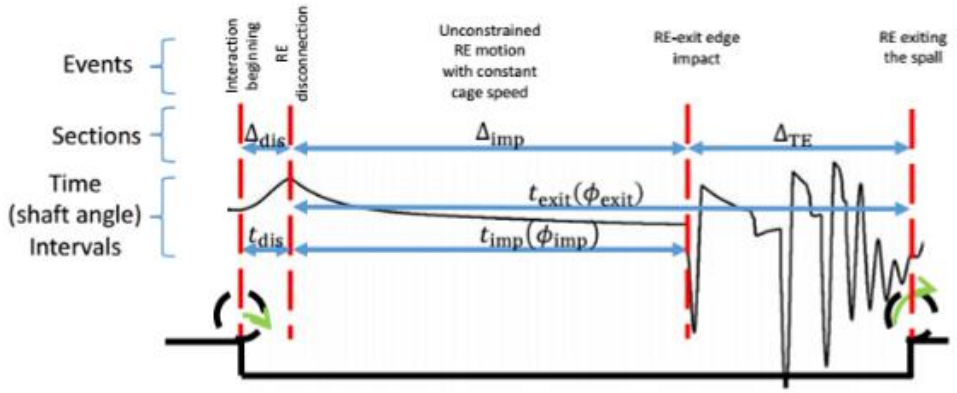


Figure 6: Time and angle intervals based on the order events [11]

The expressions in equation (4) presented below, show the relation between entrance zone, free flight and the rattling zone as function of the shaft angle-to-impact $\phi_{\text{imp}}$ :

$$\begin{Bmatrix} \Delta_s = \Delta_{dis} + \Delta_{imp} + \Delta_{TE} \\ \Delta_{dis} = \sqrt{2R_{RE}\delta} \\ \Delta_{imp} = \dfrac{\omega_c D_P}{2} t_{imp} \\ \Delta_{TE} = \sqrt{R_{RE}^2 - \left( \delta - R_{RE} + \omega_c D_p \sqrt{\dfrac{\delta}{2R_{RE}}} t_{imp} + \left( g + \dfrac{D_p}{2}\omega_c^2 \right) \dfrac{t_{imp}^2}{2} \right)^2} \\ t_{imp} = \dfrac{\phi_{imp}}{\omega_I} \end{Bmatrix} \quad (4)$$

where Δdis, Δimp, and $\Delta_{TE}$ are presented in Figure 6, $R_{RE}$ is the radius of the rolling element, δ is the initial contact deflection between the rolling element and the inner raceway, $\omega_c$ is the angular cage speed, Dp is the bearing pitch diameter, $t_{imp}$ is the time-to-impact, g is the gravity constant and $\omega_I$ is the angular shaft speed.

By analyzing equation (4) we could notice that the entrance zone, Δdis, and the rattling zone, ΔTE are related to δ, the initial contact deflection between the rolling element and the inner raceway that is influenced by the load on the rolling element.

## 4.2 Comparing healthy and faulty bearings test results

Two main periodic phenomena can be identified in the strain time history (Figure 7). Both have the same frequency, *i.e.*, the Ball Pass Frequency on the Outer ring (BPFO). One is caused by the rolling element passing over the sensor and can be observed both in a healthy bearing signal and in the faulty bearing. The second is a result of the interaction between the rolling element and the fault. Once the rolling element reaches the edge of the fault, it starts its fly over the fault area generating a sudden decrease in the outer ring strain due to the reduction of load transferred from the inner ring to the outer ring. When the rolling element exits the spall the load on the outer ring returns to its original value and the strain continues to follow the "healthy behavior" reflecting the passing rolling element. This phenomenon appeared clearly only when the

fault was located out of the loading zone. The strain behavior when the fault is located in the loading zone is discussed in paragraph 5.2.

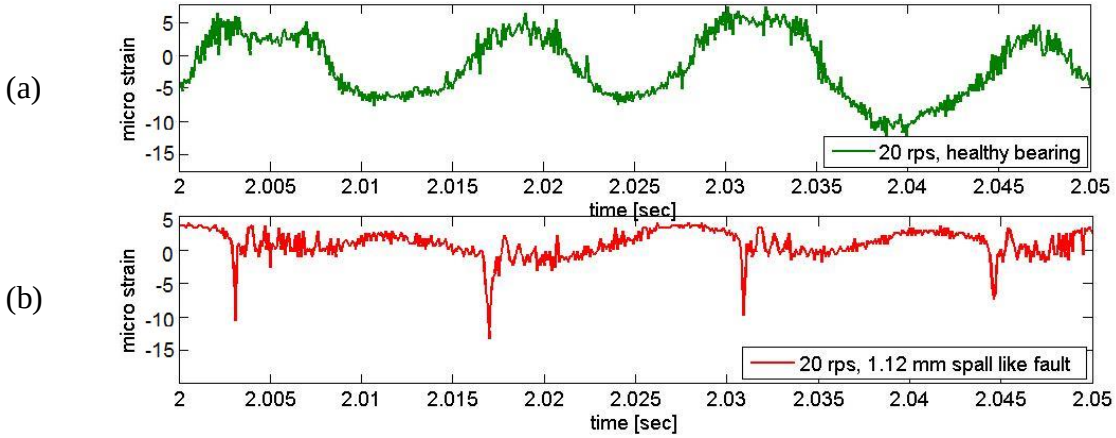


Figure 7: Strain time history comparison between a healthy bearing (a) and a 1.12mm faulty outer ring (b)

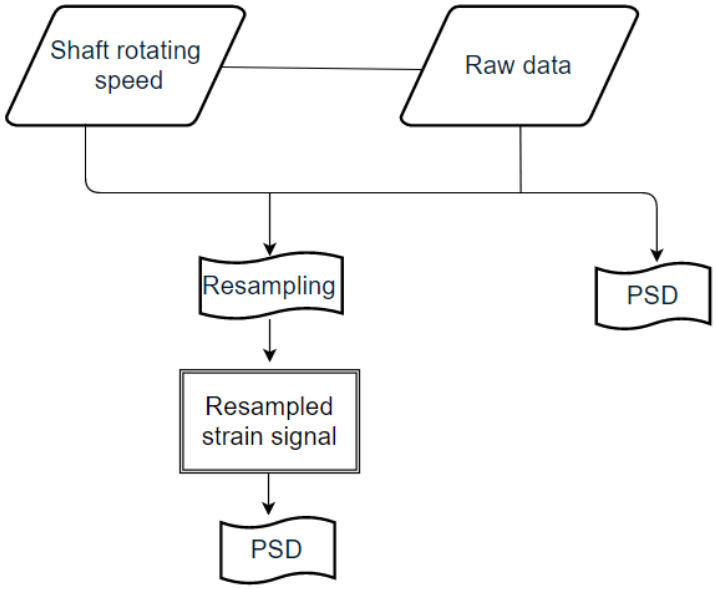


Figure 8: Analysis procedure

The signal from the FBGs was analyzed with the same techniques usually used for vibration signal processing [3]. The data analysis flow chart is described in Figure 8.

Spectra in order domain from healthy and faulty bearings were compared as shown in Figure 9. The order spectrum of the healthy bearing (green line) has peaks only at the low harmonics of the BPFO, while the order spectrum of the faulty bearing (red line) contains many peaks at high harmonics of the BPFO. Similar results were obtained for all the faulty bearings in all the conditions and experiments including all the fault locations and rotating speeds.

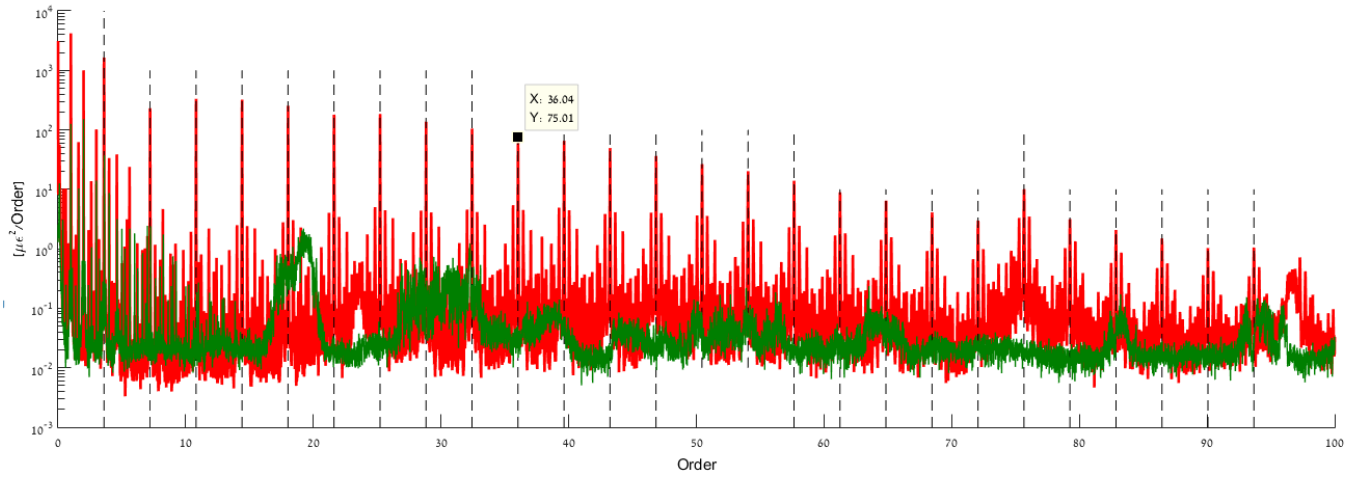


Figure 9: PSD of 1.12 mm faulty (red) and healthy (green) bearing, rotating speed 40 rps.

## 4.3 Spall detection

In order to evaluate the capability to detect the spall and to assess the reliability of detection a statistical distance (Mahalanobis) was calculated. The distance of the signal from the mean of the "healthy" population (baseline) in units of standard deviations was calculated. In this case the "healthy" population was composed of 3 measurements for each operating condition combination. The distance represents only the outer ring defect bearing spectrum, *i.e.*, values of 10 harmonics of the BPFO.

The distance P is calculated using the following formula:

$$P = \frac{\sum_{i=1}^{N}(x_i - \mu_i)}{\sqrt{\sum_{i=1}^{N}\sigma_i^2}} \qquad (5)$$

where, x is the spectrum/peak level, $\mu$ is the mean level of the baseline, $\sigma$ is the standard deviation of the baseline and N is pattern size.

Figure 10 shows the distance parameters in 12 different runs, with rotating speed of 60rps. Figure 10 presents results from three configurations S06, S07 and S08 including different measurement locations, 3 runs of the healthy bearing and similar runs of bearings with the fault on the outer race in the center of the loading zone. The sampling rate was 10 Ksample/sec.

The distance of the healthy bearing in all the measurements is below 3, while all other distances (of the faulty bearings) are above 100. It is obvious that the detection of the fault using FBG sensors is possible, promising a very good discrimination power under all the conditions and experiments, including all fault locations and rotating speeds. Additionally, the level of the statistical distance is proportional to the geometric distance between the sensor and the fault. Therefore it gives a good indication about the optimal location of the FBG sensor (as close as possible to the fault) while indicating that all the tested locations were acceptable for diagnostics.

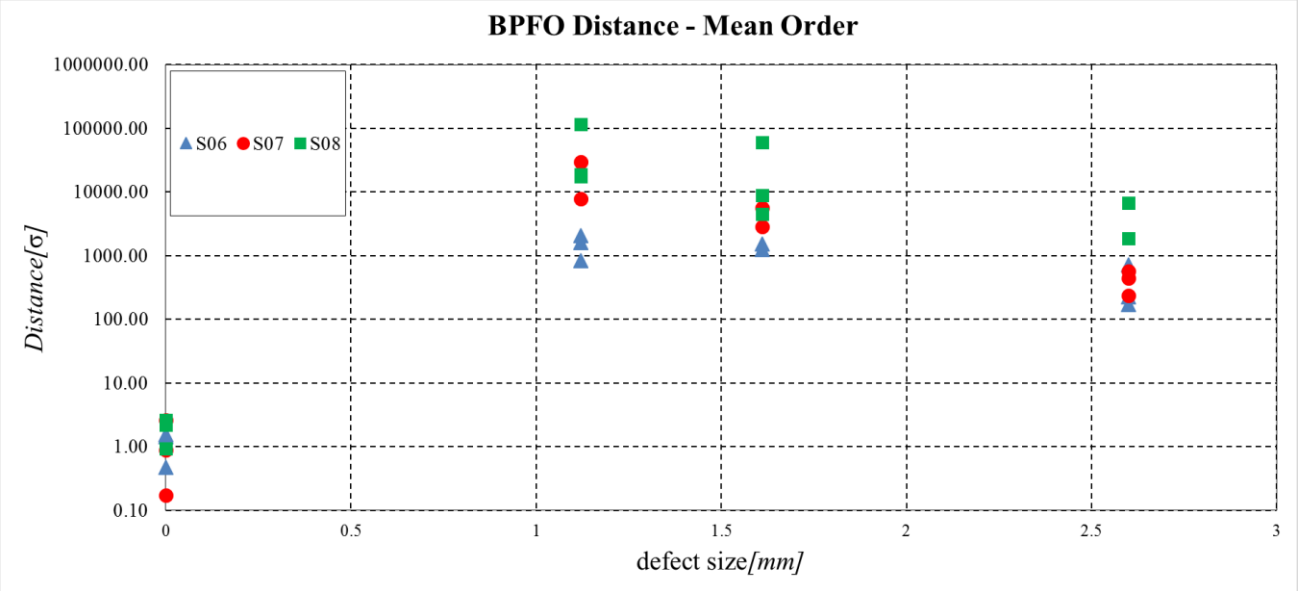


Figure 10: Distance parameter

# 5 Loading zone effect

By analyzing equation (4) we could notice that the entrance zone, Δdis, and the rattling zone, ΔTE are related to δ, the initial contact deflection between the rolling element and the inner raceway that is influenced by the loading on the rolling element. Therefore, the strain signals are expected to behave differently when the fault is located in and out the loading zone. In the loading zone we expect to see the rattling and the entrance due to the load carried by the rolling element. Out of the loading zone these phenomena may be negligible.

## 5.1 Faults out of the loading zone

Reviewing the cycle domain of the strain signals from the FBG sensors shown in Figure 11, one can observe a sudden decrease (pulse) in the strain occurring in all rotating speeds and fault widths. The sudden decrease is due to the reduction of load transferred from the inner ring to the outer ring when the rolling element performs the free flight over the fault. When the rolling element exit the spall the load on the outer ring returns to its original value, and as expected, out of the loading zone the entrance and rattling zones are negligible due to the low loads.

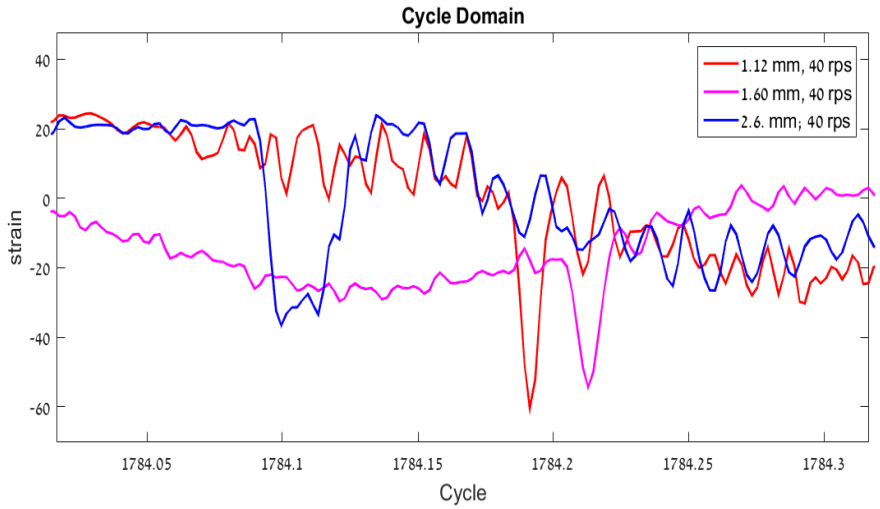


Figure 11: Comparison between different spall widths with same rotating speed on the time domain

The strain pulse width in the cycle domain during passing of the rolling element over the fault is proportional to the fault width. The relation between the bearing geometry and the pulses presented by the Defect Size Ratio (DSR):

$$DSR = \frac{\Delta X}{X} = \frac{\Delta C}{C} \tag{6}$$

where $\Delta X$ is the fault width, X is the distance between rolling elements, $\Delta C$ is the pulse width in the cycle domain and C is the distance between two pulses in the cycle domain as illustrated in Figure 12.

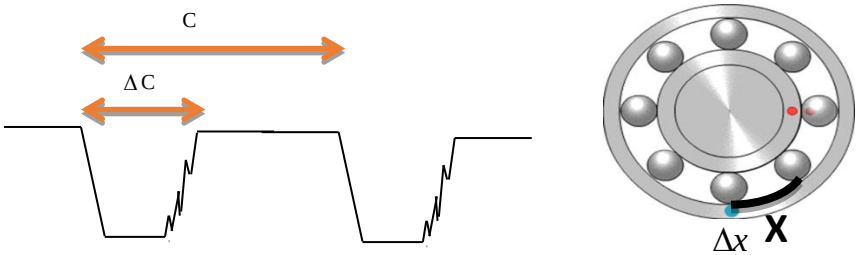


Figure 12: Defect Size Ratio illustration

The relation between C and the BPFO could be obtained by:

$$C = \frac{1}{BPFO} \tag{7}$$

X is the distance between two rolling elements and could be obtained by:

$$X = \frac{\pi(D_p + D_{RE})}{n} \tag{8}$$

where $D_p$ is the bearing pitch diameter, $D_{RE}$ is the diameter of the rolling element and n is the number of rolling elements.

Therefore, by measuring the pulse width from the strain in the cycle domain, the estimated spall size is:

$$\Delta X = \frac{BPFO \cdot \pi(D_p + D_{RE})}{n} \Delta C \tag{9}$$

The estimation of the fault width when the fault is located out of the loading zone could be achieved easily by using equation (9) and by identifying the entrance and exit points, respectively. Faults of width above 0.39 mm were estimated using this method with errors of up to 12% using a sample rate of 10 Ksample/sec and rotating speeds up to 60 rps and with an error of only 6% with rotating speed limited to 30 rps.

## 5.2 Faults in the loading zone

Most of the experiments were conducted with sampling rate of 10 Ksamples/sec. Under these conditions, major differences between the strain signals measured with the fault in and out of the loading zone were found. The cycle domain of the strain when the fault is in the loading zone did not reveal a pulse per interaction of the rolling element with the fault. The entrance and the exit of the spall corresponding to the pulse width in the cycle domain could not be determined. As expected in the loading zone, the signal from the entrance zone and the rattling zone are more significant compared to the free flight. In addition, the rattling zone contains impulses of high frequency, complicating the signal. The low sampling rate compared

with the frequency of the impacts in the rattling zone, does not allow tracking of the free flight zone of the rolling element described in paragraph 4.1. If we take as an example the experiment that was carried out with rotating speed of 40 rps and defect size of 1.6 mm, we could notice (Table 3) that the free flight time, $t_{imp} = 2.67 \times 10^{-4} \text{sec}$, sampled at 10 Ksample/sec will generate ~ 2.7 samples in the flight zone. The flight zone width is $\Delta_{imp} = 0.8$ mm, half of the defect size. Therefore, the rattling and the entrance zone will contain also ~ 2.7 samples that will not allow to track the phenomena in these conditions.

| Defect size | 1.12mm | | 1.6mm | | 2.6mm | |
|---|---|---|---|---|---|---|
| Rotation speed [rps] | $\Delta_{imp}$ [mm] | $t_{imp}$ [sec] | $\Delta_{imp}$ [mm] | $t_{imp}$ [sec] | $\Delta_{imp}$ [mm] | $t_{imp}$ [sec] |
| 20 | 0.4859 | 3.25E-04 | 0.8073 | 5.39E-04 | 1.4948 | 9.99E-04 |
| 40 | 0.4827 | 1.61E-04 | 0.8006 | 2.67E-04 | 1.4792 | 4.94E-04 |
| 60 | 0.4822 | 1.07E-04 | 0.7994 | 1.78E-04 | 1.4764 | 3.29E-04 |

Table 3: The free flight width and time calculated by equation (4) in the loading zone

Some experiments have been conducted with sample rate of 20 Ksample/sec. In these measurements the fault effect could be observed as shown in

Figure 13. Although we could not determine the entrance and the exit of the spall nor the exact area of the rattling, the width of the fault effect was found proportional to the spall width.

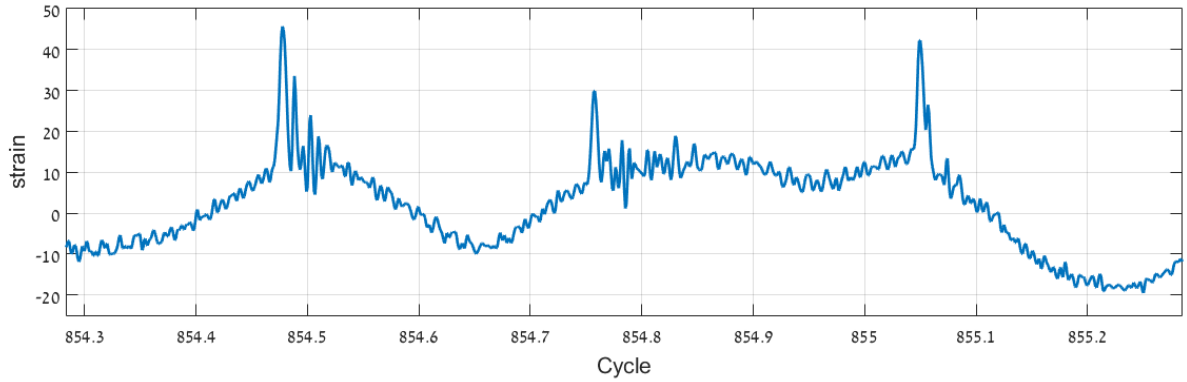


Figure 13: Strain in the cycle domain, fault width 1.12 mm, rotating speed 40 rps, sampling rate 20KHz

One of the experiments that has been held in the PHM lab in BGU (Ben-Gurion University), is an endurance test of a radially-loaded deep grove bearing. This test was performed on a different bearing type, different bearing house that was loaded radially by a pneumatic cylinder. The bearing developed a spall during the test having a fault located in the center of the loading zone. By the DSR method, it was possible to measure the growth of the fault size as a function of time. The bearing was disassembled and the generated spall was measured. The estimated spall size based on the DSR was 3.9 mm and the actual spall size was 3.89 mm. An example of the strain signal is given in Figure 14 and the photo of the actual spall in Figure 15.

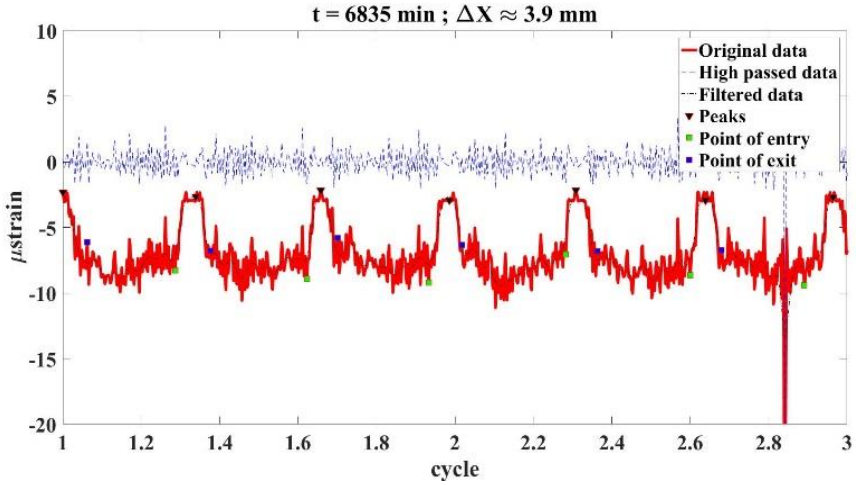


Figure 14: Size estimation of the spall size based on the DSR ratio

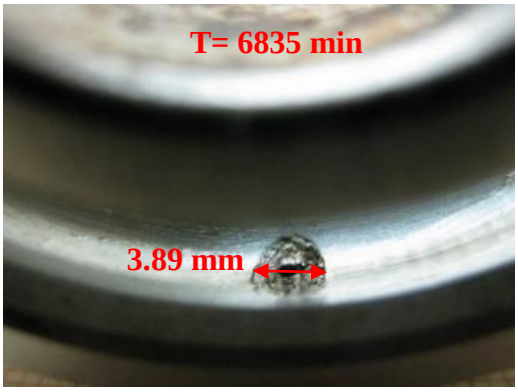


Figure 15: Bearing fault size measurement

Although the fault generated in the endurance experiment was in the loading zone, we could determine the entrance and the exit in the strain signal and calculate the fault width using the DSR method. The endurance test was conducted under different conditions including the bearing type, bearing house and loads.

# 6 Summary and conclusions

Using fiber sensors for bearing health monitoring can improve diagnostic capabilities. These sensors can be placed in the immediate proximity of bearings. The signal-to-noise ratio of the bearing strains is considerably enhanced and transmission path issues are reduced.

In the current research it was demonstrated that the optical sensor enables diagnostics of spall-like faults in the outer race with a very good discrimination power. Moreover, in some cases estimation of the fault size was possible with very high accuracy.

This demonstration is based on results of more than one hundred seeded fault experiments. The developed measurement and analysis methodology was implemented in a bearing fatigue endurance test to monitor the bearing health and estimate the damage severity.

The sensitivity to FBG sensor location was studied and it was found that at all housing measuring points, the sensitivity was acceptable. The measurement sensitivity was found to be proportional to the geometric distance between the sensor and the fault giving a good indication on the optimal location of the FBG sensor.

It was found that the fault location, inside or outside the bearing loading zone, affects the strain behavior. Outside the loading zone, the fault size can be estimated with good accuracy. There are indications that inside the loading zone, higher sampling rate will enable the fault size estimation.

Future research will be focused on better understanding of the loading zone effect, improving the measurement equipment and studying additional fault characteristics.

# Acknowledgement

We gratefully acknowledge the invaluable support of Mr. Ran Gruszkiewicz, Mr. Udi Dauber and Mr. Ilya Geiker. The vital contributions of Mr. Alex Kushnirsky and Mr. Iddo Kressel to the experimental parts of this research is highly appreciated.


## References


[1] I K Epps, 'An investigation into vibrations excited by discrete faults in rolling element bearings', PhD thesis, University of Canterbury, New Zealand, 1991.

[2] A Heng, S Zhang, A C Tan and J Mathew, 'rotating machinery prognostics: State of the art, challenges and opportunities'. Mechanical Systems and Signal Processing, vol. 23, no. 3, pp. 724–739, Apr. 2009.

[3] N Sawalhi and R B Randall, 'Semi-automated bearing diagnostics – three case studies. School of Mechanical and Manufacturing Engineering. The University of New South Wales, Sydney, Australia, 2008.

[4] G Kogan, J Bortman and R Klein. Estimation of the spall size in a rolling element bearing. Insight, Vol 57, No 8, August 2015

[5] M Khmelnitsky, J Bortman, U Ben-Simon, R Klein and M Tur, 'Improved bearing sensing for prognostics: from vibrations to optical fibres' Insight - Non-Destructive Testing and Condition Monitoring, Vol. 57, Num. 8, August 2015, pp. 437-441(5)

[6] A D Kersey, M A Davis, H J Patrick, M LeBlanc, K P Koo, C G Askins, M A Putnam and E J Friebele, 'Fiber Grating Sensors', Lightwave Technology, Journal of vol. 15, no. 8, August 1997.

[7] A Othonos and K Kalli. 'Fiber Bragg gratings: fundamentals and applications in telecommunications and sensing'. Artech House, 1999.(7)

[8] D C Betz, G Thursby, B Culshaw and W J Staszewski, 'Advanced layout of a fiber Bragg grating strain gauge rosette', Lightwave Technology, Journal of vol.24, no.2, pp.1019,1026, February 2006.(8)

[9] 'Acceleration/Vibration Tunable Lasers for Multichannel Fiber-Optic Sensors', Sensors Online, August 1, 2003. From: http://www.sensorsmag.com/sensors/acceleration-vibration/tunable-lasers-multichannel-fiber-optic-sensors-823

[10] K C Gayan, J Epaarachchi, H Wang, and K T Lau, "Use of FBG sensors for SHM in aerospace structures."

[11] G. Kogan, R. Klein, A. Kushnirsky, J. Bortman, Toward a 3d dynamic model of a faulty duplex ball bearing, Mechanical Systems and Signal Processing 54 (2015) 243–258.